

High-frequency microwave cavity design for high-mass dark matter axion searches

Chi Zhang, Jia Wang, Chunguang Li, Shiguang Chen, Hang Cheng, Liang Sun, and Yun Wu

Citation: Chin. Phys. B, 2024, 33 (**5**): 054211. DOI: 10.1088/1674-1056/ad34ca
Journal homepage: http://cpb.iphy.ac.cn; http://iopscience.iop.org/cpb

What follows is a list of articles you may be interested in

Broadband bidirectional Brillouin-Raman random fiber laser with ultra-narrow linewidth

Qian Yang(杨茜), Yang Li(李阳), Hui Zou(邹辉), Jie Mei(梅杰), En-Ming Xu(徐恩明), and Zu-Xing Zhang(张祖兴)
Chin. Phys. B, 2024, 33 (**2**): 024206. DOI: 10.1088/1674-1056/ad09cb

Tunable magnomechanically induced transparency and fast-slow light in a hybrid cavity magnomechanical system

Qinghong Liao(廖庆洪), Kun Peng(彭坤), and Haiyan Qiu(邱海燕)
Chin. Phys. B, 2023, 32 (**5**): 054205. DOI: 10.1088/1674-1056/acaf2b

Degenerate cascade fluorescence: Optical spectral-line narrowing via a single microwave cavity

Liang Hu(胡亮), Xiang-Ming Hu(胡响明), and Qing-Ping Hu(胡庆平)
Chin. Phys. B, 2021, 30 (**6**): 064211. DOI: 10.1088/1674-1056/abd76b

ontrol of microwave signals using bichromatic electromechanically induced transparency in multimode circuit electromechanical systems

Cheng Jiang(江成), Yuanshun Cui(崔元顺), Xintian Bian(边心田), Xiaowei Li(李晓薇), Guibin Chen(陈贵宾)
Chin. Phys. B, 2016, 25 (**5**): 054204. DOI: 10.1088/1674-1056/25/5/054204

Controllable optical response in hybrid opto-electromechanical systems

Jiang Cheng (江成), Cui Yuan-Shun (崔元顺), Liu Hong-Xiang (刘洪香), Li Xiao-Wei (李晓薇), Chen Gui-Bin (陈贵宾)
Chin. Phys. B, 2015, 24 (**5**): 054206. DOI: 10.1088/1674-1056/24/5/054206

Optical trapping capability of tornado circular Pearcey beams

Na-Na Liu(刘娜娜)[1], Xiao-Ying Tang(唐晓莹)[1], Shun-Yu Liu(刘舜禹)[1], and Yi Liang(梁毅)[1,2,†]

[1] *Guangxi Key Laboratory for Relativistic Astrophysics, Center on Nanoenergy Research, Guangxi Colleges and Universities Key Laboratory of Blue Energy and Systems Integration, School of Physical Science and Technology, Guangxi University, Nanning* 530004, *China*

[2] *State Key Laboratory of Featured Metal Materials and Lifecycle Safety for Composite Structures, Nanning* 530004, *China*

(Received 2 January 2024; revised manuscript received 9 March 2024; accepted manuscript online 13 March 2024)

We systemically investigate optical trapping capability of a kind of tornado waves on Rayleigh particles. Such tornado waves are named as tornado circular Pearcey beams (TCPBs) and produced by combining two circular Pearcey beams with different radii. Our theoretical exploration delves into various aspects, including the propagation dynamics, energy flux, orbital angular momentum, trapping force, and torque characteristics of TCPBs. The results reveal that the orbital angular momentum, trapping force, and torque of these beams can be finely tuned through the judicious manipulation of their topological charges (l_1 and l_2). Notably, we observe a precise control mechanism wherein the force diminishes with $|l_1+l_2|$ and $|l_1-l_2|$, while the torque exhibits enhancement by decreasing solely with $|l_1+l_2|$ or increasing with $|l_1-l_2|$. These results not only provide quantitative insights into the optical trapping performance of TCPBs but also serve as a valuable reference for the ongoing development of innovative photonic tools.

Keywords: trapping capability, tornado beams, autofocusing

PACS: 42.25.Bs, 42.50.Wk, 74.25.Uv, 87.80.Cc **DOI:** 10.1088/1674-1056/ad3347

1. Introduction

Optical tweezers, renowned for their contactless and non-damaging micromanipulation capabilities, have found extensive applications in diverse fields such as single molecule biology, biomedicine, physics, structural assembly of matter, and colloidal science.[1–3] Initially relying on fundamental Gaussian beams (GBs) for trapping, the evolving landscape of optical tweezers technology has spurred the demand for more precise manipulation and advanced photonic tools. Notably, the incorporation of structured beams,[2–7] such as optical vortices carrying orbital angular momentum (OAM), has enriched optical manipulation capabilities. These beams, resembling an "optical wrench", can effectively rotate particles within the optical tweezers system.[8–10] Intriguingly, optical vortices also create a dark optical well, minimizing photodamage in biphotonic applications of optical tweezers.[2] Building upon optical vortices, ongoing research focuses on designing novel photonic tools to enhance optical trapping performance.

In 2010, the discovery of circular Airy beams (CABs) sparked considerable interest and gave rise to abruptly autofocusing beams.[11,12] These beams possess unique characteristics that render them highly valuable in optical tweezers.[13] Autofocusing beams maintain a low intensity distribution during propagation, yet their intensity rapidly increases, forming a potent optical trap at the focal point.[13] Compared to GBs, autofocusing beams offer distinct advantages for particle manipulation, allowing precise control at lower power levels and reducing the risk of photodamage. Consequently, efforts to optimize optical manipulation performance often involve combining optical vortices with autofocusing beams, resulting in various abruptly autofocusing vortex beams.[14–19] Recently, a novel wavepacket named as tornado waves (TOWs) has been introduced, demonstrating the capability of both angular and radial acceleration.[18,20–24] This distinctive dual acceleration is achieved by combining two OAM ring-Airy or swallowtail beams with opposite signs, generating high-intensity lobes that follow a parabolic trajectory and exhibit significant angular acceleration. The extreme values of angular acceleration make TOWs promising for various applications, particularly in the realm of optical trapping. Nevertheless, the quantitative characterization of the optical trapping force magnitude of TOWs remains relatively unexplored, necessitating further research to deepen our understanding of their potential advantages and applications in optical manipulation.

Therefore, in this work, we systemically investigate optical trapping capability of a tornado circular Pearcey beam (TCPB) on Rayleigh particles in theory. Circular Pearcey beams (CPBs), a type of autofocusing beams, have been studied for their stronger autofocusing properties and better trapping performance than CABs, demonstrating an enormous potential for optical manipulations.[25,26] Here, we comprehensively examine the propagation dynamics, energy flux, orbital angular momentum (OAM), trapping force, and torque characteristics of TCPBs. Our findings conclusively demonstrate their remarkable capability for rotational trapping and manipulation of microparticles. By carefully tuning the combination of topological charges (TCs, l_1 and l_2), we can achieve precise control over the OAM, trapping force, and torque of these beams. Our analysis reveals that while the magnitude of trap-

†Corresponding author. E-mail: liangyi@gxu.edu.cn

© 2024 Chinese Physical Society and IOP Publishing Ltd

ping force diminishes with both $|l_1+l_2|$ and $|l_1-l_2|$, the torque exhibits a contrasting dependence, decreasing with $|l_1+l_2|$ but amplifying with $|l_1-l_2|$. These insights quantify the optical trapping performance of TCPBs, opening exciting avenues for the development of innovative photonic tools in optical tweezers techniques and diverse biomedical applications.

2. Theoretical background

As mentioned in Refs. [20–22], tornado waves (TOWs) can be generated by integrating two radially symmetric accelerating beams with a linear azimuthal vortex phase of opposite signs, while ensuring a slight differentiation between the two beams. Consequently, a TCPB can be produced by combining two circular Pearcey beams with different radii, as expressed by

$$\psi_{\mathrm{TCPB}}(r,0)=\sum_{i=1,2}A_0 Pe\left[\frac{(r_i-r)}{w_i},0\right]\mathrm{Tr}(r)\exp(\mathrm{i}l_i\varphi), \tag{1}$$

where A_0 represents the amplitude, $Pe(u,v)=\int_{-\infty}^{\infty}\exp[\mathrm{i}(t^4+t^2u+tv)]\mathrm{d}t$ is the Pearcey function, $r=\sqrt{x^2+y^2}$ is the radial coordinate, r_1 and r_2 are parameters that govern the initial radii of TCPB, w_1 and w_2 denote the transverse scale factors. $\mathrm{Tr}(r)=\mathrm{rect}(r/r_1)$ $(r\geqslant 0)$ serves as an indicator restricting power for practical generation, r_1 is employed to delimit the beam region, l_1 and l_2 represent the topological charges of opposite signs.

Following the utilization of Eq. (1) to define the input field distribution of the TCPBs at the initial plane, our initial step involves the numerical simulation of the paraxial propagation of TCPBs using beam propagation methods.[25,26] To ensure effective and consistent comparison of the propagation behavior, we adopted appropriate parameters to ensure that the two combined circular Pearcey beams in Eq. (1) have the same focal lengths: $r_1=150$ μm, $r_2=225$ μm, $w_1=91$ μm, $w_2=85$ μm, $\lambda=532$ nm, input power $P=1$ W. Subsequently, by adjusting the topological charges l_1 and l_2, we can effortlessly regulate the twisted propagation and trapping behaviors of TCPBs.

3. Results and discussion

3.1. Propagation dynamics of TCPBs

Figure 1 illustrates the propagation outcomes of TCPBs with various topological charges. Initially, at the starting plane, the number of main lobes of TCPBs equals the absolute difference in topological charge, denoted as $|l_1-l_2|$ [Figs. 1(a1)–1(c1)]. During propagation, TCPBs undergo an abrupt autofocusing process with clockwise rotation, transforming into minimal lobes with the highest peak intensity at the focal point $z=f=250$ mm [Figs. 1(a2)–1(c2)]. Subsequent to the focal point, the beams expand and the peak intensity diminishes rapidly [Figs. 1(a3)–1(c3)], resulting in the entire propagation resembling a tornado. Altering the sign of the topological charges reverses the rotation direction. Specifically, when $|l_1|=|l_2|$, the rotation direction depends on the sign of l_2, and the rotation speed increases with topological charge during autofocusing propagation. This is attributed to the rapid autofocusing of the Pearcey beam carrying l_2 with the larger initial radius. However, when $|l_1|\neq|l_2|$ the rotation direction relies on the sign of the difference in topological charges l_1-l_2, and the speed increases with the absolute value of the difference in topological charges $|l_1-l_2|$.

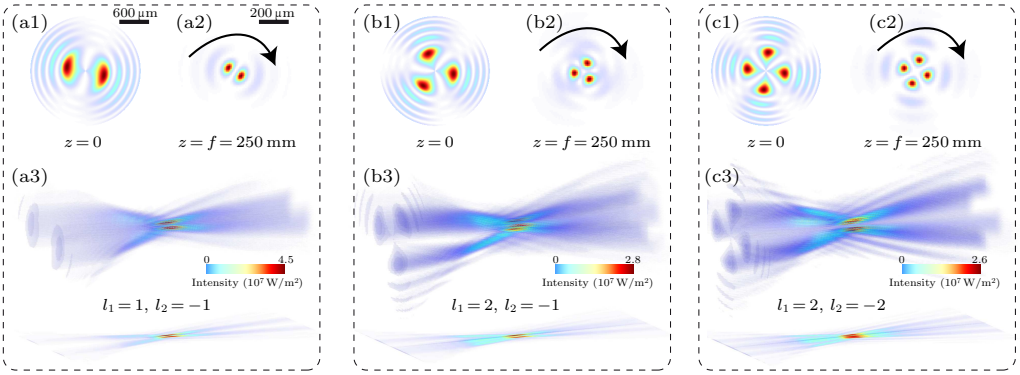


Fig. 1. Propagation of TCPBs with different topological charges: (a) $l_1=1, l_2=-1$; (b) $l_1=2, l_2=-1$; (c) $l_1=2, l_2=-2$. Intensity profiles of TCPBs: (a1)–(c1) at $z=0$ mm, (a2)–(c2) at focal plane $z=f=250$ mm; (a3)–(c3) 3D side views of propagation. The arrow indicates the direction of rotation.

3.2. Energy flux and angular momentum of TCPBs

To explain the propagation dynamics of the TCPBs, we calculate Poynting vector $\boldsymbol{S}$, which characterizes the rate of energy flow per unit area, and its direction represents the direction of the energy transfer ($\boldsymbol{S}=\boldsymbol{E}\times\boldsymbol{H}$, $\boldsymbol{E}$ and $\boldsymbol{H}$ are the electric and magnetic fields). The Poynting vector $\boldsymbol{S}$ can be expressed as[4,23,27]

$$\boldsymbol{S}_\perp=\frac{\mathrm{i}}{4\eta_0 k}[\psi\nabla_\perp\psi^*-\psi^*\nabla_\perp\psi], \tag{2}$$

where $\boldsymbol{S}_\perp$ indicates the transverse component of the Poynting vector, $\eta_0=\sqrt{\mu_0/\varepsilon_0}$ is the impedance of free space,

$k = 2\pi n/\lambda$ is the wave number, $\nabla_\perp = \frac{\partial}{\partial x}\boldsymbol{e}_x + \frac{\partial}{\partial y}\boldsymbol{e}_y$ is the gradient operator, the asterisk represents the complex conjugate.

Figure 2 presents the energy flux characteristics of TCPBs while varying the topological charges. At the initial plane, a significant portion of the transverse Poynting vector points towards the middle region, causing energy convergence and initiating an autofocusing propagation [Figs. 2(a1)–2(c1)]. However, due to the presence of a phase vortex, there is a small region with a clockwise Poynting vector distribution at the beam center, as depicted in the insets of Figs. 2(a1)–2(c1). As the propagation continues, energy gradually shifts towards the center, leading to an increase in the transverse Poynting vector. Yet, before reaching the focus, some power from the center begins to flow outward. Despite this, the total incoming power remains greater than the outgoing power at the center of TCPBs. Upon reaching the focus, there is no net energy flux into the center, and the Poynting vector becomes zero at the most central position [Figs. 2(a2)–2(c2)]. In Fig. 2(a2), there appears to be a noticeable rotation of energy flow concentrated at the center. Conversely, in Fig. 2(b2), the energy flow manifests as three distinct smaller vortices surrounding the center. Furthermore, in Fig. 2(c2), the predominant aspect of the energy flow appears to be radial, emanating outward from the center. Consequently, the peak intensity of TCPBs reaches its maximum value. At this moment, the rotation also reaches its maximum, and the Poynting vector for $|l_1| \neq |l_2|$ is larger than that for $|l_1| = |l_2|$, indicating a quicker rotation, as introduced in Fig. 1. Moreover, Poynting vector surrounding the center for $|l_1| \neq |l_2|$ undergoes a transformation to an anticlockwise direction. Simultaneously, it exhibits a clockwise distribution when observed from alternative three axis-systemic positions, implying a complex rotational energy flux. After focus, the Poynting vector around the center continues to increase, and all the transverse Poynting vectors near the center change their direction from inside to outward. This shift results in input power being less than output power, causing a decrease in peak intensity and outward diffusion of the main lobe. Eventually, all Poynting vectors point outwards, signifying power outflow (see more detail from supplementary videos 1–3).

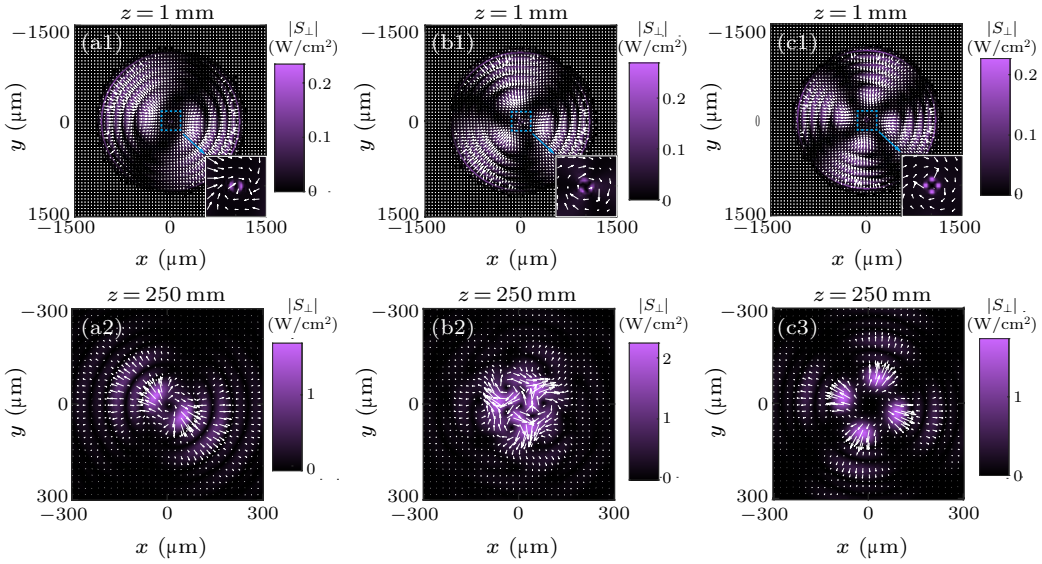


Fig. 2. Transversal energy flux distributions corresponding to Fig. 1: (a) $l_1 = 1, l_2 = -1$; (b) $l_1 = 2, l_2 = -1$; (c) $l_1 = 2, l_2 = -2$.

Likewise, owing to the presence of topological charges in TCPBs, a spiral wavefront is generated, imparting OAM to the beam and enabling the rotation of small particles. As we know, OAM quantifies the rotational state of an object, making it a suitable descriptor for the rotational characteristics of TCPBs. To perform a quantitative analysis of the OAM in TCPBs, we delved into the study of the angular momentum density (AMD) of TCPBs. The longitudinal AMD of TCPBs is theoretically calculated by[23,27]

$$j_z = (\boldsymbol{r} \times \boldsymbol{p})_z = (r \times (\boldsymbol{E} \times \boldsymbol{H})/c^2)_z, \tag{3}$$

where $\boldsymbol{p}$ represents the linear momentum density. Then, the total OAM J_z can be obtained by integrating the longitudinal AMD j_z across the entire space. This can be expressed mathematically as $J_z = \iint j_z \mathrm{d}x\mathrm{d}y$. Thus, the OAM per photon $\langle l \rangle$ is

$$\langle l \rangle = \frac{J_z w}{P} = cw \frac{\iint j_z \mathrm{d}x\mathrm{d}y}{\iint S_z \mathrm{d}x\mathrm{d}y}, \tag{4}$$

where w stands for angular frequency.

Figure 3 illustrates the distribution of longitudinal AMD of TCPBs with the topological charges $l_1 = 1, l_2 = -1$, $l_1 = 2$, $l_2 = -1$, $l_1 = 2, l_2 = -2$. At the initial plane, only TCPBs with topological charges $|l_1| \neq |l_2|$ exhibit the largest AMD. When $|l_1| = |l_2|$, the opposite topological charges l_1 and l_2, cancel each other out, resulting in a relatively small but nonzero longitudinal AMD [Figs. 3(a1)–3(c1)]. Consequently, the beams

can still undergo rotation. Similarly, at the focal plane, the AMD for TCPBs with $|l_1| \neq |l_2|$ possesses the largest OAM and the strongest trapping capability for spiral rotation. Following the passage through the focus, the AMD of TCPBs gradually decreases as the propagation continues (see more detail from supplementary videos 4–6).

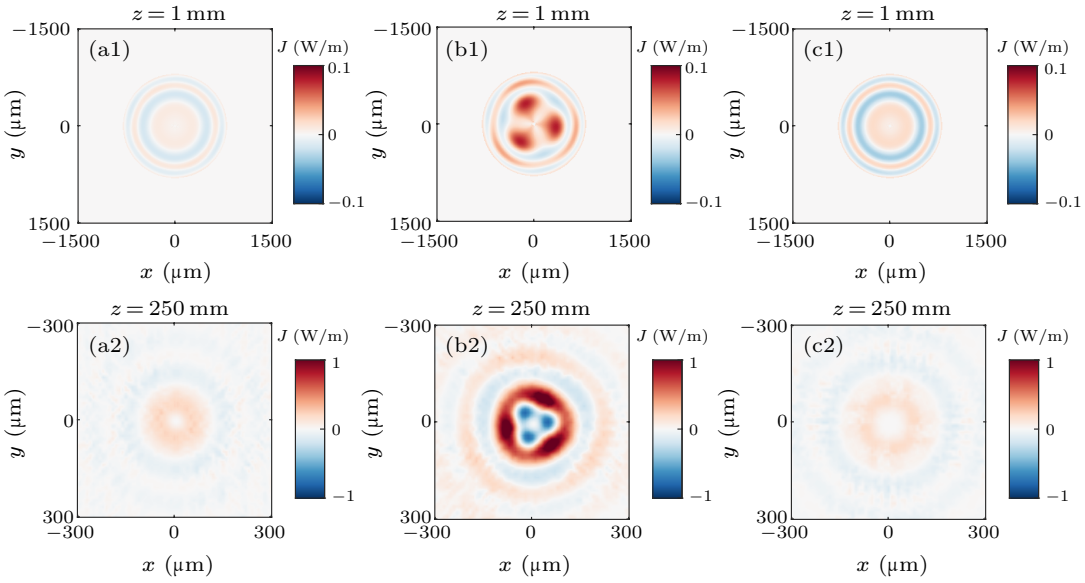


Fig. 3. Longitudinal AMD distributions corresponding to Fig. 1: (a) $l_1 = 1, l_2 = -1$; (b) $l_1 = 2, l_2 = -1$; (c) $l_1 = 2, l_2 = -2$.

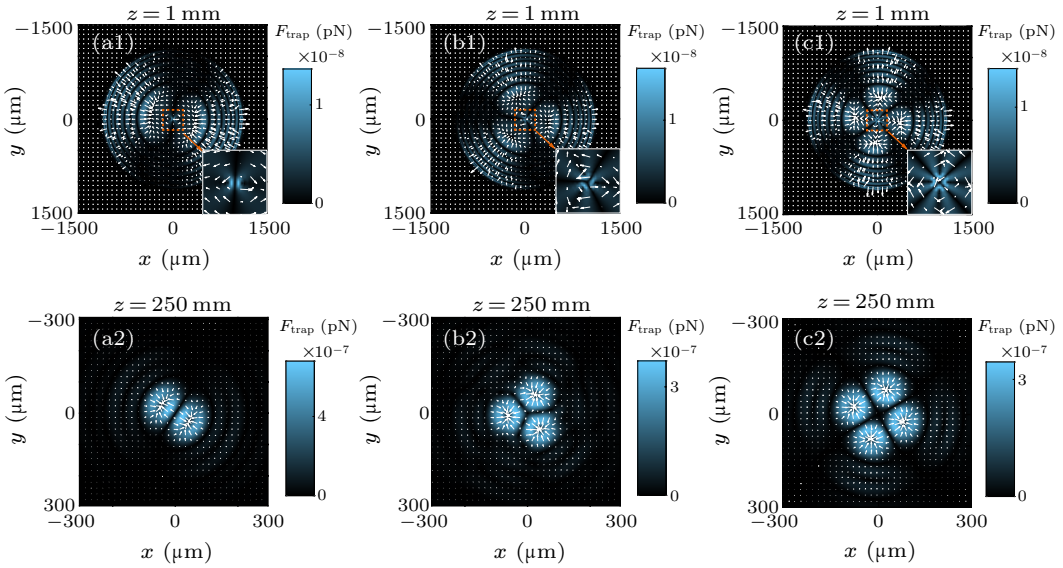


Fig. 4. Transversal trapping force distributions corresponding to Fig. 1: (a) $l_1 = 1, l_2 = -1$; (b) $l_1 = 2, l_2 = -1$; (c) $l_1 = 2, l_2 = -2$.

3.3. Optical trapping force and torque of TCPBs

The autofocusing characteristics and spiral propagation of TCPBs play a crucial role in optical trapping and manipulation. In the subsequent analysis, we delve into the trapping forces exerted on a Rayleigh polystyrene particle (50 nm) in water, encompassing the gradient force F_g and scattering force F_s:[4,17]

$$F_g = \frac{1}{4}\varepsilon_0\varepsilon_m R_e(\alpha)\nabla|\psi^2|,$$
$$F_s = \frac{1}{6\pi c}\varepsilon_m^3 k_0^4 |\alpha|^2 S, \tag{5}$$

where ε_0 is the permittivity in vacuum, $\alpha = 4\pi R^3(\varepsilon_p - \varepsilon_m)/(\varepsilon_p + 2\varepsilon_m)$ is the polarizability, R is the radius of the particle, c is the light speed in vacuum, $\varepsilon_p = 2.5$ and $\varepsilon_m = 1.7$ are the dielectric permittivities of particle and medium, respectively.

To analyze the trapping characteristics of TCPBs, we simulated the distribution of trapping force at the initial position and focal position ($\boldsymbol{F}_{trap} = \boldsymbol{F}_g + \boldsymbol{F}_s$), as illustrated in Fig. 4. At the initial plane, the maximum trapping force peak of TCPBs is localized on the main lobes, with the force vectors directed towards the dark region at the center of the main lobe [Figs. 4(a1)–4(c1)]. Additionally, trapping positions manifest

on the other annular lobes from the inside to the outside, accompanied by a gradual decrease in trapping force. As the propagation unfolds, the peak trapping force at each distance from the initial plane increases before reaching the focal point, where it attains its maximum and achieves the most stable trapping. The trapping force at the focal point surpasses that at the initial plane by one order of magnitude and is directed towards the center of the main lobe of the TCPBs. Notably, in Fig. 4(a2) with the least value of $|l_1|+|l_2|$, its trapping force is the largest due to the power being concentrated into the fewest number of main lobes. Subsequent to passing the focus, the trapping force gradually diminishes (refer to supplementary videos 7–9 for details). It is important to emphasize that trapping force is intimately related to intensity, and thus, the fluctuating trend of the force aligns with that of peak intensity in Fig. 1. In this context, the positions of trapping force exhibit a consistent rotation pattern during propagation, mirroring the behavior of Fig. 1 and the trajectories of trapped particles.

To delve further into the study of the effect of TCPBs on rotating particles, we also conducted a detailed investigation of the optical trapping torque, which represents the tendency of a force to induce the rotation of particles about an axis. The formula for optical trapping torque is given by[28]

$$\boldsymbol{M} = \boldsymbol{r} \times \boldsymbol{F}_{\text{trap}}. \tag{6}$$

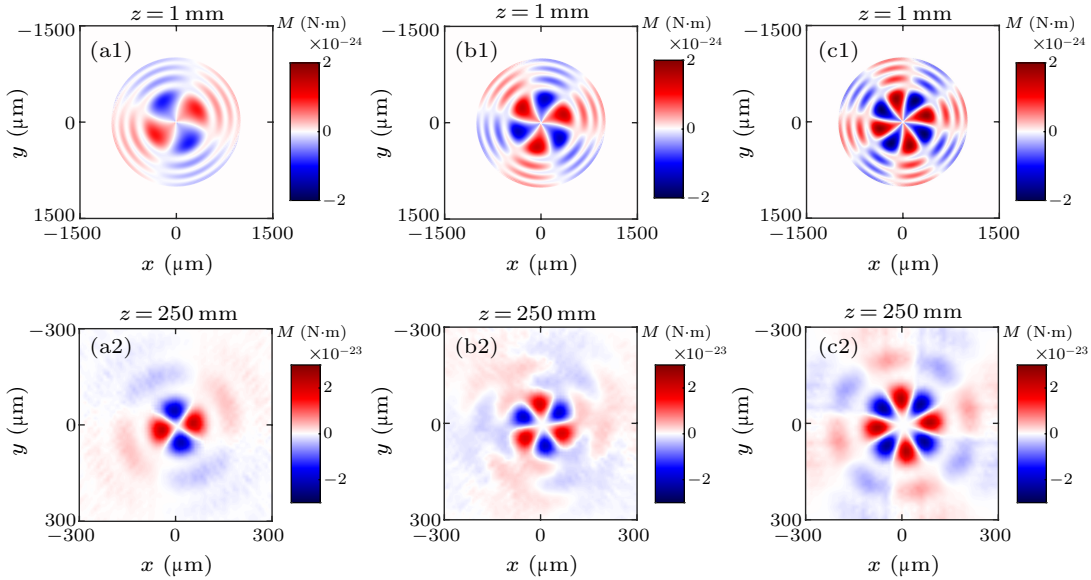


Fig. 5. Optical trapping torque distributions corresponding to Fig. 1: (a) $l_1 = 1$, $l_2 = -1$; (b) $l_1 = 2$, $l_2 = -1$; (c) $l_1 = 2$, $l_2 = -2$.

Figure 5 illustrates the distribution of trapping torque exerted by TCPBs with different topological charges. As depicted in Fig. 4, at the initial plane, the forces in each lobe do not align in the same direction, resulting in both positive and negative torque symmetrically occurring in each lobe in Fig. 5. In this scenario, particles are consistently trapped in the center of the lobes, precisely at the midpoint between positive and negative torques [Figs. 5(a1)–5(c1)]. With the propagation of TCPBs, the torque steadily increases. Upon reaching the focus, the torque reaches its maximum value, showcasing an order of magnitude larger torque than at the initial plane. This enhancement allows for greater rotational torque at the focus [Figs. 5(a2)–5(c2)]. Following the passage through the focus, the torque experiences a rapid decrease (refer to supplementary videos 10–12 for details). Throughout the entire propagation process, the optical trapping torque consistently exhibits rotation concurrent with trapping force. The combined action of force and torque ensures that captured particles are not only securely bound to the center of the light spot but also rotate in tandem with the center's rotation, enabling precise manipulation by beam. It is noteworthy that, in all the cases, the torque increases with the values of the difference of topological charges $|l_1 - l_2|$.

Typically, the optical trapping torque is computed to illustrate the rotational influence of the field on nanoparticles. To enhance clarity in demonstrating this effect, we select the trapping center as the reference point for torque calculation. In Figs. 4(a2)–4(c2), where there are 2, 3, and 4 trapping centers, respectively, we consistently utilize the lower right corner trapping center as the origin. This choice yields the results depicted in Fig. 6, effectively illustrating the rotational dynamics induced by the optical field.

3.4. Discussion

The above findings from our investigations consistently indicate that TCPBs possess a superior trapping capability, revealing their potential for precise optical rotation manipulation through the strategic modulation of their topological charges. To further analyze such rotational trapping perfor-

mance, we embarked on a quantitative exploration to scrutinize the changes in OAM, trapping force, and torque in response to variations in topological charges (l_1, l_2, l_1+l_2, and l_1-l_2) at focal plane.

Figure 7(a) presents the variation of OAM in TCPBs with topological charges l_1 and l_2. The three diagonal yellow dashed lines represent l_1+l_2 equals -5, 0, and 5, respectively. Notably, the OAM exhibits a negative maximum at the bottom left corner and gradually transitions into a positive maximum as it progresses towards the top right corner. Specifically, as depicted in Fig. 7(a2), the OAM linearly gets larger with the increase of l_1+l_2. At $l_1+l_2=0$, the OAM nearly approaches 0. Conversely, Fig. 7(a3) depicts the variation of OAM with l_1-l_2. Moving from the bottom row to the top row, the OAM also exhibits a linear increase, aligning with the OAM values from the bottom left to the top right of Fig. 7(a1). It is noteworthy that when $l_1-l_2<0$, the negative and positive OAMs increase with l_1-l_2, presenting an opposite trend compared to the case of $l_1-l_2>0$.

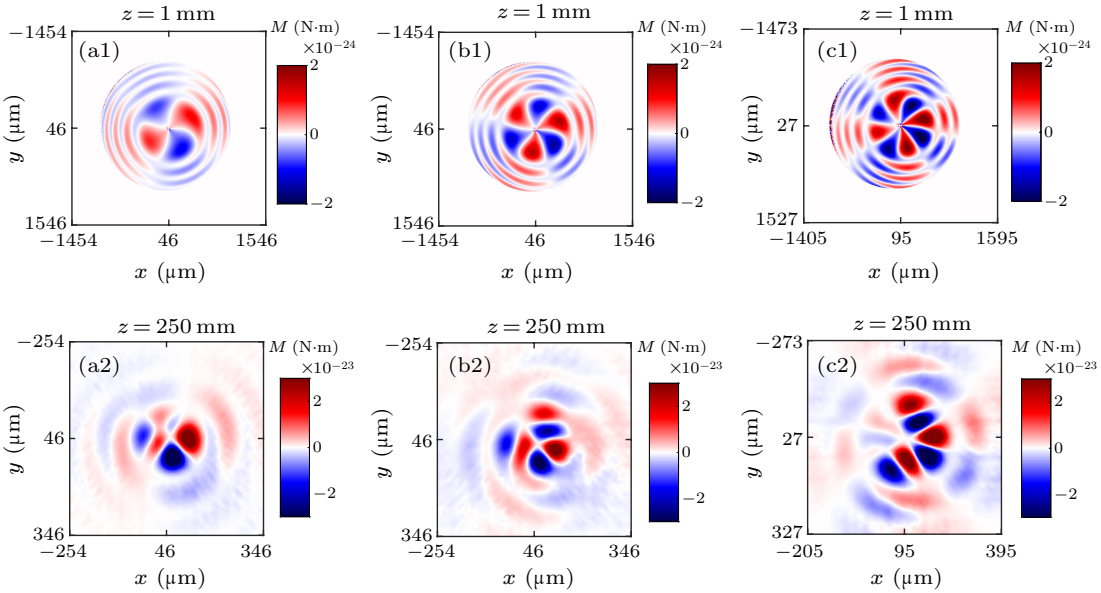


Fig. 6. Optical trapping torque distributions (choosing the trapping centers as the origin) corresponding to Fig. 1: (a) $l_1=1$, $l_2=-1$; (b) $l_1=2$, $l_2=-1$; (c) $l_1=2$, $l_2=-2$.

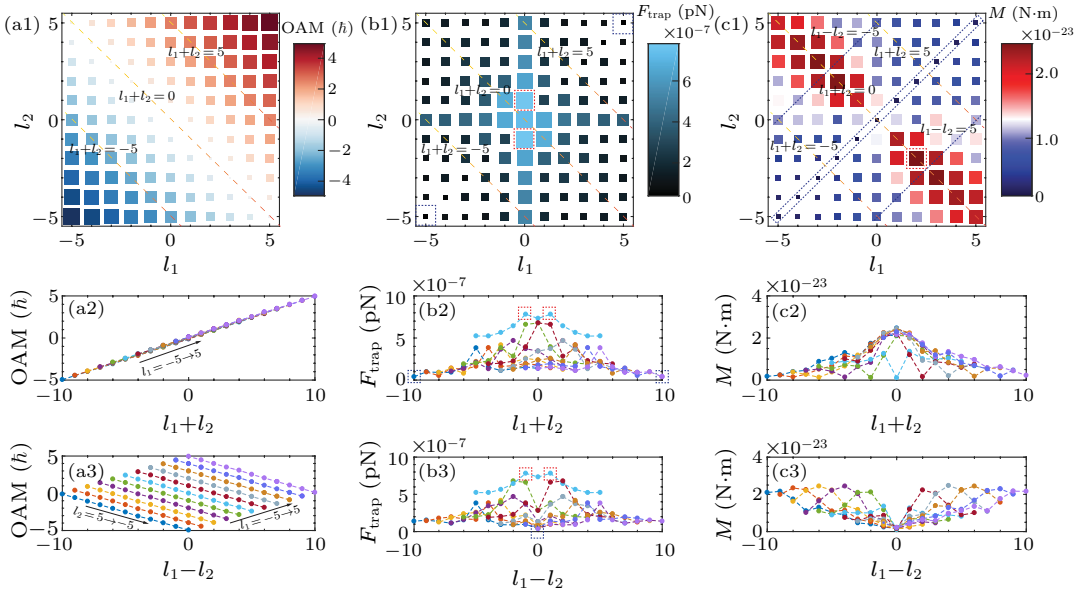


Fig. 7. Variation of OAM, trapping force, and torque of TCPBs with topological charges l_1, l_2, l_1+l_2, and l_1-l_2 at focal plane: (a) OAM; (b) trapping force; (c) torque. Variations (a1)–(c1) with l_1 and l_2, (a2)–(c2) with l_1+l_2, (a3)–(c3) with l_1-l_2.

Figure 7(b1) depicts the variation of trapping force for TCPBs with topological charges l_1 and l_2. Clearly, the proximity to the center of the cross corresponds to a larger trapping force. In Fig. 7(b2), each color signifies the trapping force associated with each column in Fig. 7(b1) concerning the change in l_1+l_2. The red dashed box aligns with $l_1=0$,

$l_2 = 1, -1$, representing the configuration where trapping force is maximum, while the blue dashed box corresponds to $l_1 + l_2 = 5, -5$, where the trapping force is minimum. Similarly, in Fig. 7(b3), each color signifies the trapping force for each column in Fig. 7(b1) as a function of $l_1 - l_2$, with the trapping force reaching its maximum in the column where $l_1 = 0$. The red dashed box and the blue dashed box still represent the maximum and minimum of trapping force. It is evident that the force exhibits similar trends with both $l_1 + l_2$ and $l_1 - l_2$. As $l_1 + l_2$ or $l_1 - l_2$ increases, the force initially rises until reaching $l_1 + l_2 = 0$ or $l_1 - l_2 = 0$, after which it descends.

Figure 7(c1) illustrates the variation of torque of TCPBs with topological charges l_1 and l_2, showing that proximity to the top left and bottom right corners corresponds to a larger torque. In Figs. 7(c2) and 7(c3), each color represents the torque variation for each column in Fig. 7(c1) concerning the change in $l_1 + l_2$ and $l_1 - l_2$. It can be observed that the torque increases with $l_1 + l_2$ first and then decreases after $l_1 + l_2 = 0$. The changes in torque with $l_1 - l_2$ exhibit an opposite trend. Specifically, the torque is maximum at $l_1 + l_2 = 0$, corresponding to the yellow dashed line in Fig. 7(c1) where $l_1 + l_2 = 0$. In this line, as $|l_1 - l_2|$ decreases from 10 to 0, the torque initially increases and reaches a maximum at $|l_1 - l_2| = 4$. Subsequently, the torque decreases and reaches a minimum at $l_1 - l_2 = 0$, corresponding to the blue dashed long square box in Fig. 7(c1), where $l_1 - l_2 = 0$.

4. Conclusions

In summary, through theoretical analysis, we have delved into the intricate dynamics of tornado circular Pearcey beams, exploring aspects such as their propagation dynamics, energy flux characteristics, orbital angular momentum, trapping force, and torque properties. The findings collectively underscore the exceptional rotational trapping and manipulation capabilities exhibited by TCPBs. Remarkably, we observe that the orbital angular momentum, trapping force, and torque of these beams can be finely tuned by manipulating the combination of their topological charges. The force demonstrates a diminishing trend with the absolute values of $|l_1 + l_2|$ and $|l_1 - l_2|$, while the torque exhibits a more intricate behavior, decreasing solely with $|l_1 + l_2|$ and escalating with $|l_1 - l_2|$. These results illuminate the intricate relationship between the topological charges and the trapping properties of TCPBs, contributing to the understanding of TCPBs as effective tools for optical trapping and manipulation. Moreover, the tunability of their force and torque characteristics opens avenues for the development of novel photonic tools.

Acknowledgments

Project supported by the National Natural Science Foundation of China (Grant No. 11604058), the Guangxi Natural Science Foundation (Grant Nos. 2020GXNSFAA297041 and 2023JJA110112), and the Innovation Project of Guangxi Graduate Education (Grant No. YCSW2023083).

References

[1] Xin H B, Li Y C, Liu Y C, Zhang Y, Xiao Y F and Li B J 2020 *Adv. Mater.* **32** 2001994
[2] Bunea A and Gluckstad J 2019 *Laser Photon. Rev.* **13** 1800227
[3] Yang Y J, Ren Y X, Chen M Z, Arita Y and Rosales-Guzmán C 2021 *Adv. Photon.* **3** 034001
[4] Liang Y, Tan L, Liu N N, Chen K J, Liang H P, Wu H H, Luo B S, Lu F X, Chen H H, Zou B S and Hong P L 2023 *Phys. Rev. Appl.* **19** 014016
[5] He C, Shen Y J and Forbes A 2022 *Light Sci. Appl.* **11** 205
[6] Lu F X, Wu H, Liang Y, Tan L, Tan Z F, Feng X, Hu Y, Xiang Y X, Hu X B, Chen Z G and Xu J J 2021 *Phys. Rev. A* **104** 043524
[7] Lu F X, Tan L, Tan Z F, Wu H H and Liang Y 2021 *Phys. Rev. A* **104** 023526
[8] Bai Y H, Lv H R, Fu X and Yang Y J 2022 *Chin. Opt. Lett.* **20** 012601
[9] Shen Y J, Wang X J, Xie Z W, Min C J, Fu X, Liu Q, Gong M L and Yuan X C 2019 *Light Sci. Appl.* **8** 90
[10] Yao A M and Padgett M J 2011 *Adv. Opt. Photon.* **3** 161
[11] Papazoglou D G, Efremidis N K, Christodoulides D N and Tzortzakis S 2011 *Opt. Lett.* **36** 1842
[12] Chremmos I, Efremidis N K and Christodoulides D N 2011 *Opt. Lett.* **36** 1890
[13] Efremidis N K, Chen Z G, Segev M and Christodoulides D N 2019 *Optica* **6** 686
[14] Jiang Y F, Huang K K and Lu X H 2012 *Opt. Express* **20** 18579
[15] Wang F L and Liang Y 2021 *Opt. Commun.* **484** 126681
[16] Wang F L, Lou C B and Liang Y 2018 *Chin. Opt. Lett.* **16** 110502
[17] Tan L, Liu N N, Lu F X, Liu D M, Yu B B, Li Y T, Wu H, Chen K J, Chu Y Z, Hong P L and Liang Y 2023 *Phys. Rev. A* **107** 043501
[18] Yang Y Z, Wu Y, Zheng X Q, Shi J Y, Luo Y J, Huang J H and Deng D M 2023 *Opt. Lett.* **48** 3535
[19] Zhang X H, Wang F L, Bai L Y, Lou C B and Liang Y 2020 *Chin. Phys. B* **29** 064204
[20] Brimis A, Makris K G and Papazoglou D G 2020 *Opt. Lett.* **45** 280
[21] Jiang J J, Xu D L, Mo Z W, Cai X Z, Huang H Y, Zhang Y, Yang H B, Huang H Q, Wu Y, Shui L L and Deng D M 2022 *Opt. Express* **30** 11331
[22] Mansour D, Brimis A, Makris K G and Papazoglou D G 2022 *Phys. Rev. A* **105** 053514
[23] Zhang Y, Tu J L, He S L, Ding Y P, Lu Z L, Wu Y, Wang G H, Yang X B and Deng D M 2022 *Opt. Express* **30** 1829
[24] Brimis A, Makris K G and Papazoglou D G 2023 *Opt. Express* **31** 27582
[25] Chen X Y, Deng D M, Zhuang J L, Peng X, Li D D, Zhang L P, Zhao F, Yang X B, Liu H Z and Wang G H 2018 *Opt. Lett.* **43** 3626
[26] Lu X F, Tan L, Liu N N, Chen C W, Chen K J, Wu H X, Xia X S, Zhang P Y, Hong P L, Zou B S and Liang Y 2023 *Phys. Rev. A* **108** 063509
[27] Dorrah A H, Rosales-Guzmán C, Forbes A and Mojahedi M 2018 *Phys. Rev. A* **98** 043846
[28] Jones P, Marago O M and Volpe G 2015 *Optical Tweezers: Principles & Applications* (Cambridge: Cambridge University Press) p. 139